Journal of Energy Chemistry 37 (2019) 7–12

Contents lists available at ScienceDirect

Journal of Energy Chemistry

journal homepage: www.elsevier.com/locate/jechem

http://www.journals.elsevier.com/journal-of-energy-chemistry/

Integrated Co_3O_4/carbon fiber paper for high-performance anode of dual-ion battery

Lu Sui, Xiaoyuan Shi, Ting Deng, He Yang, Hongyan Liu, Hong Chen, Wei Zhang*, Weitao Zheng*

Key Laboratory of Mobile Materials MOE, School of Materials Science & Engineering, Electron Microscopy Center, International Center of Future Science, Jilin University, Changchun 130012, Jilin, China

ARTICLE INFO

Article history:
Received 13 October 2018
Revised 7 November 2018
Accepted 10 November 2018
Available online 22 November 2018

Keywords:
Integrated electrode
Dual-ion batteries
Co_3O_4
Anode
Carbon fiber paper

ABSTRACT

In dual-ion batteries (DIBs), energy storage is achieved by intercalation/de-intercalation of both cations and anions. Due to the mismatch between ion diameter and layer space of active materials, however, volume expansion and exfoliation always occur for electrode materials. Herein, an integrated electrode Co_3O_4/carbon fiber paper (CFP) is prepared as the anode of DIB. As the Co_3O_4 nanosheets grow on CFP substrate vertically, it promotes the immersion of electrolyte and shortens the pathway for ionic transport. Besides, the strong interaction between Co_3O_4 and CFP substrate reduces the possibility of sheet exfoliation. An integrated-electrode-based DIB is therefore packaged using Co_3O_4/CFP as anode and graphite as cathode. As a result, a high energy density of 72 Wh/kg is achieved at a power density of 150 W/kg. The design of integrated electrode provides a new route for the development of high-performance DIBs.

1. Introduction

Dual-ion batteries (DIBs) with the virtues of wide voltage window, high safety and low cost, show the potential in the field of electrochemical energy storage [1–5]. Both anions and cations from DIB electrolyte are involved in charge/discharge process, and the anions insertion has a high voltage (~4.5 V vs. Li/Li^+) while the ions transport possesses fast kinetics, which endows DIBs with the concurrence of high power density and high energy density [6–10]. To accommodate ions, materials with layer structure, such as graphite and MXene, can be used as the electrode in DIBs [2,11–14]. However, this remains a great challenge for maintaining the stability of DIBs, as it suffers from the unavoidable mismatch of ion radii and interlayer spacing of host materials. Volume change of electrode material is severe which can even trigger exfoliation, resulting in the degradation of cycling and the overall performance [15–18].

Efforts have been made to address the critical issue. On one hand, nanosizing of active material can effectively release internal stress and shorten the ion transfer path within their layered structure [19–21]. For example, Zhu et al. prepared three-dimensional (3D) ultrathin porous Co_3O_4 nanoparticles with high surface area and well-developed mass-transportation channels. Nano-sized Co_3O_4 achieves high stability and high rate simultaneously. On the other hand, materials with 3D cross-link network or hierarchical structure are preferred to enhance the cycling performance of electrode [22–25]. Xiong et al. synthesized the nanometer-sized Co_3O_4 array on 3D porous Ni skeleton by electrodepositing and solvent heating method [26]. Such integrated electrode without conductive and adhesive agents provides a capacity of 714 mAh/g and maintains 90% after 100 cycles. Nevertheless, the random orientation of active materials limits the permeation of electrolyte and lowers the utilization of overall material [27,28]. In the case of layered materials, some planar surfaces are mutually covered causing the shrinkage of gap spacing, which can be the bottleneck to further unlock the full potential of DIBs. Moreover, the transition metal oxides obtain higher capacity than traditional graphite anode for dual-ion batteries [29].

Herein, we propose a facile strategy to prepare a highly oriented and binder-free Co_3O_4/CFP (carbon fiber paper) electrode by electrochemical deposition as the anode for DIB, which obtains a capacity of ~530 mAh/g at a current density of 200 mA/g. The Co_3O_4/CFP electrode holds over 90% capacity after 40 cycles. The Coulombic efficiency is close to 100% after the first five cycles. Furthermore, a DIB is therefore fabricated with Co_3O_4/CFP, graphite

* Corresponding authors.
E-mail addresses: weizhang@jlu.edu.cn (W. Zhang), wtzheng@jlu.edu.cn (W. Zheng).

https://doi.org/10.1016/j.jechem.2018.11.009

and $LiPF_6$ as integrated anode, cathode and electrolyte, respectively. This DIB shows a high energy density of 72 Wh/kg in a working window of 2∼4 V (vs. Li/Li^+). Our integrated electrode preparation method not only improves the overall performance of the DIB, but also provides a new route for the commercial development of battery technology.

2. Experimental

2.1. Synthesis of Co_3O_4/CFP electrode

CFP was ultrasonically cleaned by acetone, ethanol and deionized water for 30 min, respectively. The perpendicular $Co(OH)_2$ flower-like nanosheets were electrochemically deposited on CFP in 0.1 M $Co(NO_3)_2$ aqueous solution. Then the Co_3O_4/CFP composite electrode was obtained through high temperature calcination method. The as-prepared $Co(OH)_2$/CFP composite was put in the oven at 60 °C for 8 h and then transferred to a tube furnace (SKGL-1200) transforming from $Co(OH)_2$/CFP into Co_3O_4/CFP. The rate of heating was 5 °C/min under the air flow up to 450 °C and then stayed for 2 h. The prepared Co_3O_4/CFP integrated electrode was prepared in a vacuum drying oven for 12 h, and the water in the electrode was completely removed.

2.2. Structural characterization

The phase structure measurements of $Co(OH)_2$/CFP and Co_3O_4/CFP were carried out on X-ray diffraction (XRD, RIGAKU D/MAX2500) using Cu $K\alpha$ radiation ($\lambda = 1.5406$ Å). The morphologies of $Co(OH)_2$/CFP and Co_3O_4/CFP were observed by a field emission scanning electron microscope (SEM, Hitachi SU8010). The composition of samples was determined by X-ray energy dispersive spectrum (EDS, ESCALAB-250 performed with a monochromatic Al $K\alpha$ radiation source and a hemisphere detector with an energy resolution of 0.1 eV). The particle size and the dispersion degree of Co_3O_4 on the CFP were verified using a transmission electron microscope (TEM, JEM-2100F). The X-ray photoelectron spectroscopy (XPS) was detected for the binding energy between $Co(OH)_2$, Co_3O_4/CFP and CFP, which were performed with a monochromatic Al $K\alpha$ radiation source (ESCALAB-250) and a hemisphere detector with an energy resolution of 0.1 eV.

2.3. Electrochemical measurements

We used CHI660E (CH instrument, Shanghai) electrochemical workstation to conducted electrochemical measurements, which consist of cyclic voltammetry, galvanostatic charge–discharge curves. Electrochemical impedance spectroscopy (EIS) was invested by PARSTAT 2273, with the AC signal amplitude of 10 mV test frequencies ranging from 0.01 to 100,000 Hz. Electrochemical charge-discharge behavior was examined using coin cells (type CR2032) assembled in an argon-filled glove box. The half-cell test was conducted by using an integrated electrode Co_3O_4/CFP (anode) and graphite (cathode) as working electrodes, Li foil as counter electrode. The potential window of the integrated electrode Co_3O_4/CFP half-cell is from 0.5 to 3 V (vs. Li/Li^+). Then the DIBs were matched according to the principle of equal electric quantity of two single electrodes. The electric quantity equals to capacity multiply time. We tested graphite and Co_3O_4 electrodes respectively to select two with equal electric quantity and integrate to build DIBs. DIB test was conducted by Co_3O_4/CFP as anode, graphite as cathode and polypropylene film as separator in 1 M $LiPF_6$ solution, and the working window is 2–4 V. The calculation formulas of energy density (E, Wh/kg) and power density (P, W/kg) were calculated according to the following equations:

$$E = CV \tag{1}$$

$$P = E/t \tag{2}$$

where C (mAh/g) is the capacity of discharge and V (V) is the median voltage; t (s) is the discharge time. For the full-cell, m (g) is the total mass of the positive and negative active materials. As can be seen from the formula, the capacity and voltage determine the energy density of the battery.

3. Results and discussion

The schematic illustration of synthesis for Co_3O_4/CFP composition is shown in Fig. 1(a). First, $Co(OH)_2$ is immersed in the $Co(NO_3)_2$ aqueous solution and then the electrodeposition is conducted. The electrodeposition is a productive method to prepare electrode material with uniform orientation [30,31]. Consider the semiconductor nature of Co_3O_4, the increase of thickness may induce decrease of rate capacity. So proper deposition time has been

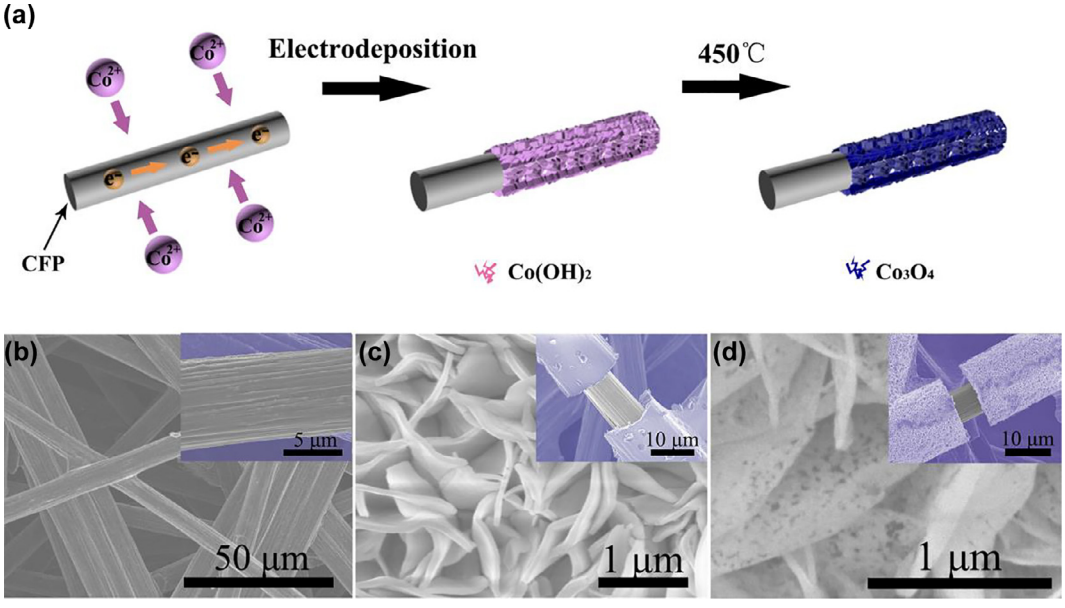

Fig. 1. (a) Illustration of preparation for Co_3O_4/CFP composition. SEM images of (b) original CFP, (c) $Co(OH)_2$/CFP and (d) Co_3O_4/CFP.

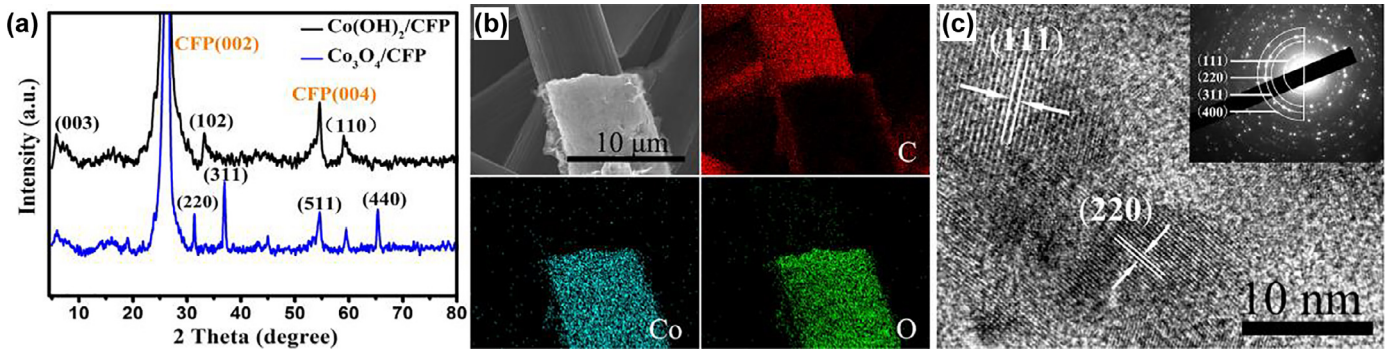

Fig. 2. (a) XRD patterns of $Co(OH)_2$/CFP and Co_3O_4/CFP. (b) EDS elemental mapping of Co_3O_4/CFP and (c) HRTEM image of Co_3O_4/CFP (inset: electron diffraction pattern).

chosen [32]. Then, the Co_3O_4/CFP composite is obtained by calcining $Co(OH)_2$/CFP through a high temperature treatment, and the CFP remains stable at this temperature (Fig. S1). The reaction mechanisms are as follows [18]:

$$NO_3^- + 7\,H_2O + 8\,e^- \rightarrow NH_4^+ + 10\,OH^- \quad (3)$$

$$Co^{2-} + 2\,OH^- \rightarrow Co(OH)_2 \quad (4)$$

$$6\,Co(OH)_2 + O_2 \rightarrow 2\,Co_3O_4 + 6\,H_2O \quad (5)$$

Morphological and microstructure changes between CFP, $Co(OH)_2$ and Co_3O_4 are investigated by SEM [33,34]. Fig. 1(b) shows the unprocessed CFP with its randomly-overlapped carbon fibers, which displays a 3D crossing-linking structure and abundant space. After the electrodepositing, $Co(OH)_2$ grows vertically on CFP with a flower-like morphology (Fig. 1c). The flower-like $Co(OH)_2$ is evenly distributed on CFP with a porous structure, and the $Co(OH)_2$ sheets are as thin as 10 nm [33]. After calcination, Co_3O_4/CFP composite still maintains the vertical structure (Fig. 1d). The average height of each petal of nanosheet is ~4.5 μm and remains unchanged after calcining (Figs. S2 and S3). The nano-pores are uniformly distributed on the Co_3O_4 nanosheets due to the escape of H and O from the surface in the process of calcination (the inset in Fig. 1d). The existence of pores enables the Co_3O_4/CFP composite to form a porous three-dimensional structure with abundant internal space and large surface area. Such unique morphology can expose more electrochemical active sites and facilitate connection between internal active material and electrolyte, which increases the utilization ratio of electrode [35,36].

X-ray powder diffraction (XRD) test was measured to analyze the crystallization of $Co(OH)_2$/CFP and Co_3O_4/CFP composites. As shown in Fig. 2(a), the diffraction peaks at 11.6°, 34.4°, 60°, and 65° can be indexed to the (003), (102), (110), and (116) planes of α-$Co(OH)_2$ (JGPDS No.30-0443). After calcinations, the composite shows the peaks at 36.9°, 59.6° and 65.5°, which can be indexed to (311), (511), and (440) planes of Co_3O_4 (PDF card No. 42-1467) [37]. The diffraction peaks of Co_3O_4 display higher intensities than those of $Co(OH)_2$, indicating higher crystallinity of Co_3O_4 than that of $Co(OH)_2$. Among the diffraction peaks of Co_3O_4/CFP, (311) plane shows the highest intensity which indicates that Co_3O_4 preferentially grew along <311> direction. The high-intensity sharp diffraction peaks at 26.6° and 54.8° corresponding to the typical (002) and (004) of graphite structure in CFP [16]. EDS was also conducted to probe the elemental distribution of C, Co, and O elements (Fig. 2b). The C element mainly exists in the CFP support, while Co and O elements are well distributed in Co_3O_4 [33]. The high-resolution transmission electron microscopy (HRTEM) image shown in Fig. 2(c) clearly exhibits the lattice fringe of Co_3O_4/CFP composite. The (111) and (220) planes (ca. 4.67 and 2.86 Å) can be observed in Co_3O_4 [38]. And the selected area electron diffraction (SAED) is given in Fig. 2(c) inset, where the distinct lattice fringe with an interlayer spacing is calculated as 0.244 Å corresponding to the largest exposed facet (311) planes. This fits well with the previous XRD analysis.

Transition metal oxide (TMO) anodes have a higher lithium storage capacity (theoretical capacity of cobalt oxide is 890 mAh/g) than graphite anode [39]. As a kind of TMO with high capacity, Co_3O_4 has been widely utilized for Li storage. Thus, Co_3O_4 served as the anode of DIB. In this work, to investigate the electrochemical properties of the Co_3O_4/CFP anode for DIB, half-cell using Li foil as both counter and reference electrodes was assembled. Fig. 3(a) shows the cyclic voltammogram curves of the initial three cycles and the potential window is set as 0.5–3 V (vs. Li/Li^+) [40]. In the first cycle, a reduction peak is observed at 0.75 V. The formation of Co and Li_2O can be described by the electrochemical reaction: $Co_3O_4 + 8Li^+ + 8e^- \leftrightarrow 4\ Li_2O + 3Co^0$ [41]. In the second and third cycles, the cathodic peak shifts to 1.10 V, the original cathodic peak disappears, and the area and strength of peak decreases. In the first three cycles, the oxide peak does not show significant change, and remains at the location of 2.15 V. The electrochemical performance of the Co_3O_4/CFP integrated electrode is basically stable from the third cycle. And the galvanostatic charge/discharge curves at a current density of 0.1 A/g are displayed in the Fig. 3(b). The behavior correlated well with the cyclic voltammograms results, and the redox reaction peak corresponded to the platform ranging from 0.5 to 3 V. The initial discharge and charge capacity are 954 and 1092 mAh/g respectively with a reasonable Coulombic efficiency (CE%) of 87.4%. The lower CE% in the first cycle may be attributed to the formation of SEI film on the surface of Co_3O_4/CFP electrode. In the second and third cycles, the charge and discharge capacity is 940 and 927 mAh/g, respectively. After the third cycle, CE% increases to 98.6% which indicates the high reversibility of Co_3O_4/CFP. To further understand the influence of SEI layer on electrochemical performance, EIS with different charge-discharge cycles is conducted (Fig. S4). The radius of semicircle in high-frequency of Nyquist curve increases after five cycles compared with the uncycled one. This can be explained that the SEI film is generated during the first cycle, which induces a high resistance. In addition, the Co_3O_4/CFP electrode shows good rate capability at various current densities between 50 and 500 mA/g (Fig. 3c). When the current density increases from 50 to 150, 250 and 500 mA/g, the discharge capacity reduces from 766 to 602, 489 and 385 mAh/g (the average values). When the current density comes back to 50 mA/g, the electrode recovers to a discharge capacity of 662 mAh/g. The integrated electrode shows minor capacity loss (13%) and superior rate performance due to conductive ion transport pathway [42]. The cycling stability of Co_3O_4/CFP electrode at a current density of 200 mA/g is given in Fig. 3(d). The integrated electrode possesses high capacity retention and the good capacity.

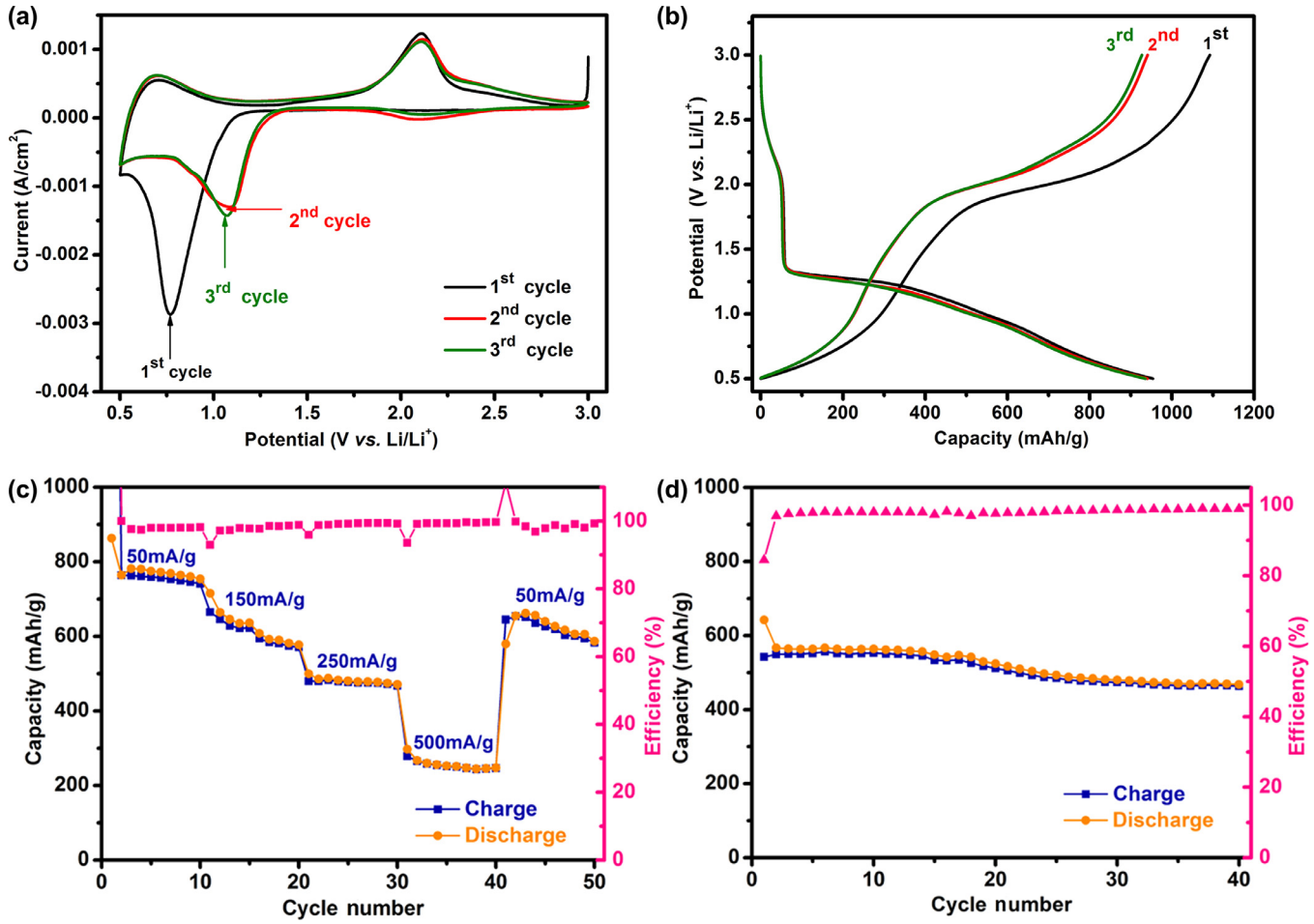

Fig. 3. The electrochemical performance of Co_3O_4/CFP integrated electrode. (a) Cyclic voltammetry curves of different charge–discharge cycles. (b) Galvanostatic charge–discharge curves of different cycles. (c) Rate capacity and Coulombic efficiency and (d) cycling stability.

The capacity of the first circle is 542 mAh/g, and it maintains over 90% after 40 cycles. The integrated Co_3O_4/CFP electrode shows as high Coulombic efficiency as almost 100% after the fifth cycle.

In order to explore the connection between active material Co_3O_4 and substrate CFP, XPS is measured. Fig. S5(a) is the C 1*s* XPS spectrum of pure CFP, which can be divided into five components: C–C, C=C bonds at 283.9, 282 eV, C–O, C=O and –HO–C=O bonds at 285.8, 288.7 and 290.1 eV, respectively. When it turns to Co_3O_4/CFP sample, besides the previous five peaks, –C–[O–Co]$_2$ and –C–[O–Co]$_3$ bonds exist at 294.1 and 297.6 eV [25,30,31]. The XPS results confirm the formation of strong chemical bonds between electrochemical active material and substrate, which benefits the cycling stability of Co_3O_4/CFP integrated electrode [37,43,44]. Fig. S6 shows superior performance in cycling stability and capacity of integrated Co_3O_4/CFP electrode than that of traditional prepared Co_3O_4 electrode. The flower-like morphology is kept almost the same before and after cycling (Fig. S7). The structure stability and tight adhesion ensure the cycling stability. The in-situ synthesis method preserves the original morphology and vertical orientation of the precursor $Co(OH)_2$, which facilitates electrolyte better infiltrate into the active materials and shortens the ion transport pathway. Thus, the electrochemical deposition followed by in-situ calcination used here is a productive electrode preparation method [45].

To obtain high energy and power densities, the anode and cathode of DIB must be delicately chosen and matched in proportion [6,46,47]. Graphite is proved to be anion intercalation host and cathode of DIBs. Fig. S8(a) shows the capacity and cycling performance of graphite as cathode in DIBs. The mass specific capacity reaches 40 mAh/g, and remains almost 100% after 50 cycles. It can be seen from Fig. S8(b) that graphite has a good rate capability, and the discharge capacity is 50, 41, 38, 35 and 50 mA/g under the current density of 20, 50, 100, 20 mAh/g, respectively. In the 50th charge-dischage circle, the Coulombic efficiency is as high as over 98% (Fig. S9).

A well-designed DIB is prepared by integrated Co_3O_4/CFP anode, graphite cathode and $LiPF_6$ electrolyte. The operating window of the DIB is 2–4 V (vs. Li/Li$^+$). Fig. 4(a) is the schematic illustration of the energy storage mechanism in the charge/discharge process of the DIB. When the DIB is charged, Li$^+$ cations react with the Co_3O_4/CFP anode, while the PF_6^- anions insert into the graphite layers [48]. When it turns to discharge process, ions come back into electrolyte. The galvanostatic charge–discharge curves at different current densities are shown in Fig. 4(b). It can be seen that the shape of different curves is bascically unchanged, revealing the good reversible of DIB. When the current density is 10, 50 and 100 mA/g, the DIB yields the discharge capacity of 24, 10 and 5 mAh/g, respectively. Fig. 4(c) is the cycling stability of the assembled DIB at a current density of 10 mA/g. After 50 cycles, the capacity remains 64%. The electrochemical performance clearly indicates that the DIB with well-designed integrated electrodes has unique advantages. That makes the DIB battery light in weight and

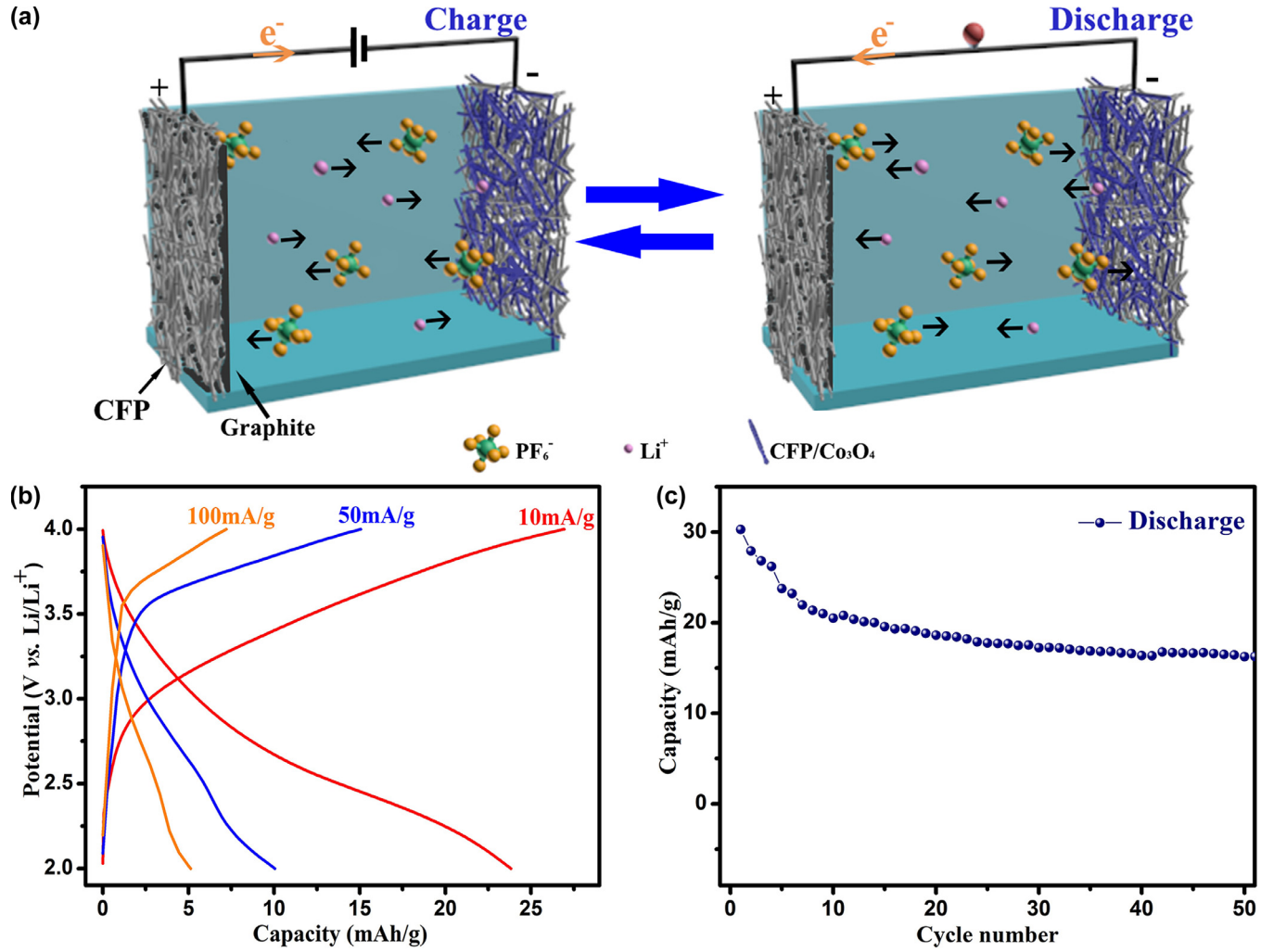

Fig. 4. (a) Charging/discharging mechanism of DIB. (b) Galvanostatic charge–discharge curves at different current densities. (c) The corresponding cycling performance of the DIB in a current densitiy of 10 mA/g.

producing high specific energy. Compared with conventional prepared Co_3O_4, the Co_3O_4/CFP has a unique structure, which is the main reason for its stability. The integration of electrode materials and current collector effectively avoids the negative influences of conductive agent and binder on the performance of electrode. And the Co_3O_4 nanosheets grow orientatedly on CFP substrate. As a result, sufficient active sites are exposed for Li^+ reaction. Thus, the integrated electrode delivers high discharge capacity. Moreover, the strong adhesion between active materials and substrate effectively aviods the exfolitation of Co_3O_4 sheets from substrate and ensures the integrity of the ion transport channel. And the loose structure of Co_3O_4 could buffer the expansion of volume caused by ion insertion, shorten the lithium ion transmission channel and then improve the performance of the battery. As a result, the excellent cycling stability of integrated electrode is achieved. To sum up, the novelly designed configuration of DIB provides a broader insight and bright commercial prospect for battery technology.

4. Conclusions

Co_3O_4/CFP integrated electrode is fabricated as high-performance anode for DIB due to its unique 3D structure and excellent cyclability. The integrated electrode can buffer the volume expansion caused by ion charge/discharge process, which effectively improves the electrochemical performance. Matching with graphite cathode and $LiPF_6$ electrolyte, the assembled DIB gains an energy density of 72 Wh/kg at a power density of 150 W/kg. This work provides a convenient and effective way for synthetic electrode materials in DIB.

Acknowledgments

Supports from the National Natural Science Foundation of China (51872115 and 51802110), the National Key R&D Program of China (2016YFA0200400), the Jilin Province/Jilin University Co-construction Project-Funds for New Materials (SXGJSF2017-3, Branch-2/440050316A36), the Program for JLU Science and Technology Innovative Research Team (JLUSTIRT, 2017TD-09), and "Double-First Class" Discipline for Materials Science & Engineering, are greatly acknowledged.

Supplementary materials

Supplementary material associated with this article can be found, in the online version, at doi:10.1016/j.jechem.2018.11.009.

References

[1] T. Ishihara, Y. Yokoyama, F. Kozono, H. Hayashi, J. Power Sources 196 (2011) 6956–6959.
[2] J.A. Read, A.V. Cresce, M.H. Ervin, K. Xu, Energ. Environ. Sci. 7 (2014) 617–620.
[3] X. Shi, W. Zhang, J. Wang, W. Zheng, K. Huang, H. Zhang, S. Feng, H. Chen, Adv. Energy Mater. 6 (2016) 1601378.
[4] Q. Li, Y. Qiao, S. Guo, K. Jiang, Q. Li, J. Wu, H. Zhou, Joule 2 (2018) 1134–1145.
[5] N. Li, Y. Xin, H. Chen, S. Jiao, H. Jiang, W.-L. Song, D. Fang, J. Energy Chem. doi:org/10.1016/j.jechem.2018.03.003.
[6] X. Tong, F. Zhang, B. Ji, M. Sheng, Y. Tang, Adv. Mater. 28 (2016) 9979–9985.
[7] X. Zhang, Y. Tang, F. Zhang, C.-S. Lee, Adv. Energy Mater. 6 (2016) 1502588.
[8] E.J. Zhang, W. Cao, B. Wang, X.Z. Yu, L.L. Wang, Z. Xu, B.G. Lu, Energy Storage Mater. 11 (2018) 91–99.
[9] G. Wang, M. Yu, J. Wang, D. Li, D. Tan, M. Loeffler, X. Zhuang, K. Muellen, X. Feng, Adv. Mater. 30 (2018) 1800533.
[10] J. Lang, X. Zhang, B. Liu, R. Wang, J. Chen, X. Yan, J. Energy Chem. 27 (2018) 43–56.
[11] J. Dahn, J. Seel, J. Electrochem. Soc. 147 (2000) 892–898.
[12] Q. Pan, H. Wang, Y. Jiang, J. Mater. Chem. 17 (2007) 329–334.
[13] M. Lu, W. Han, H. Li, W. Shi, J. Wang, B. Zhang, Y. Zhou, H. Li, W. Zhang, W. Zheng, Energy Storage Mater. 16 (2019) 163–168.
[14] A.M. Horgan, D.A. King, Trans. Faraday Soc. 67 (1971) 11355–11361.
[15] T. Placke, G. Schmuelling, R. Kloepsch, P. Meister, O. Fromm, P. Hilbig, H.-W. Meyer, M. Winter, Z. Anorg, Allg. Chem. 640 (2014) 1996–2006.
[16] J.A. Read, J. Phy. Chem. C 119 (2015) 8438–8446.
[17] J. Huesker, L. Froböse, A. Kwade, M. Winter, T. Placke, Electrochim. Acta 257 (2017) 423–435.
[18] H. Yang, X. Shi, T. Deng, T. Qin, L. Sui, M. Feng, H. Chen, W. Zhang, W. Zheng, ChemElectroChem. doi:10.1002/celc.201801108.
[19] H. Wu, Y. Cui, Nano Today 7 (2012) 414–429.
[20] M. Srivastava, J. Singh, T. Kuila, R.K. Layek, N.H. Kim, J.H. Lee, Nanoscale 7 (2015) 4820–4868.
[21] W. Xia, A. Mahmood, R.Q. Zou, Q. Xu, Energy Environ. Sci. 8 (2015) 1837–1866.
[22] D.R. Rolison, J.W. Long, J.C. Lytle, A.E. Fischer, C.P. Rhodes, T.M. McEvoy, M.E. Bourg, A.M. Lubers, Chem. Soc. Rev. 38 (2009) 226–252.
[23] Y. Huang, H.F. Li, Z.F. Wang, M.S. Zhu, Z.X. Pei, Q. Xue, Y. Huang, C.Y. Zhi, Nano Energy 22 (2016) 422–438.
[24] C.J. Chen, Y. Zhang, Y.J. Li, Y.D. Kuang, J.W. Song, W. Luo, Y.B. Wang, Y.G. Yao, G. Pastel, J. Xie, L.B. Hu, Adv. Energy Mater. 7 (2017) 1700595.
[25] D. Ji, H. Zhou, Y. Tong, J. Wang, M. Zhu, T. Chen, A. Yuan, Chem. Eng. J 313 (2017) 1623–1632.
[26] Q.Q. Xiong, H.Y. Qin, H.Z. Chi, Z.G. Ji, J. Alloys Compd. 685 (2016) 15–21.
[27] J. Luo, J. Liu, Z. Zeng, C.F. Ng, L. Ma, H. Zhang, J. Lin, Z. Shen, H.J. Fan, Nano Lett. 13 (2013) 6136–6143.
[28] K. Cao, L. Jiao, H. Liu, Y. Liu, Y. Wang, Z. Guo, H. Yuan, Adv. Energy Mater. 5 (2015) 1401421.
[29] S. Wang, J. Tu, J. Xiao, J. Zhu, S. Jiao, J. Energy Chem. (2018), doi:10.1016/j.jechem.2018.07.010.
[30] T. Deng, Y. Lu, W. Zhang, M. Sui, X. Shi, D. Wang, W. Zheng, Adv Energy Mater. 8 (2018) 1702294.
[31] D.H. Ha, M.A. Islam, R.D. Robinson, Nano Lett. 12 (2012) 5122–5130.
[32] H.X. Wang, W. Zhang, N.E. Drewett, H.B. Zhang, K.K. Huang, S.H. Feng, X.L. Li, J. Kim, S. Yoo, T. Deng, S.J. Liu, D. Wang, W.T. Zheng, J. Microscopy 267 (2017) 34–48.
[33] T. Deng, W. Zhang, O. Arcelus, J.-G. Kim, J. Carrasco, S.J. Yoo, W. Zheng, J. Wang, H. Tian, H. Zhang, X. Cui, T. Rojo, Nat. Commun. 8 (2017) 15194.
[34] H.Y. Tan, B.Z. Yu, L.L. Cao, T. Cheng, X.L. Zheng, X.H. Li, W.L. Li, Z.Y. Ren, J. Alloys Compd. 696 (2017) 1180–1188.
[35] Y. Li, L. Kong, M. Liu, W. Zhang, L. Kang, J. Energy Chem. 26 (2017) 494–500.
[36] Y. Shen, J. Mater. Chem. A 3 (2015) 13114–13188.
[37] H. Wang, D. Wang, T. Deng, X. Zhang, C. Zhang, T. Qin, D. Cheng, Q. Zhao, Y. Xie, L. Shao, H. Zhang, W. Zhang, W. Zheng, J. Power Sources 399 (2018) 238–245.
[38] Y. Tan, Q. Gao, C. Yang, K. Yang, W. Tian, L. Zhu, Sci. Rep. 5 (2015) 12382.
[39] S.-H. Park, W.-J. Lee, Carbon 89 (2015) 197–207.
[40] J. Chen, J.Z. Wang, A.I. Minett, Y. Liu, C. Lynam, H. Liu, G.G. Wallace, Energy Environ. Sci. 2 (2009) 393.
[41] Z.S. Wu, W. Ren, L. Wen, L. Gao, J. Zhao, Z. Chen, G. Zhou, F. Li, H.M. Cheng, ACS Nano. 4 (2010) 3187–3194.
[42] M.A. Islam, M. Zuba, V. DeBiase, N. Noviasky, C.J. Hawley, Nanotechnology 29 (2018) 075403-075403.
[43] Y. Jiang, L. Chen, H. Zhang, Q. Zhang, W. Chen, J. Zhu, D. Song, Chem. Eng. J. 292 (2016) 1–12.
[44] S. Liu, T. Deng, X. Hu, X. Shi, H. Wang, T. Qin, X. Zhang, J. Qi, W. Zhang, W. Zheng, Electrochim. Acta 289 (2018) 319–323.
[45] S.-K. Park, A. Jin, S.-H. Yu, J. Ha, B. Jang, S. Bong, S. Woo, Y.-E. Sung, Y. Piao, Electrochim. Acta 120 (2014) 452–459.
[46] C. Jiang, Y. Fang, J. Lang, Y. Tang, Adv. Energy Mater. 7 (2017) 1700913.
[47] S. Zhang, M. Wang, Z. Zhou, Y. Tang, Adv. Funct. Mater. 27 (2017) 1703035.
[48] X. Shi, T. Deng, B. Zhang, W. Zhang, L. Sui, H. Yang, D. Wang, W. Shi, C.-M. Chen, W. Zheng, ChemElectroChem 4 (2017) 3238–3243.